RSC Advances

PAPER

View Article Online
View Journal | View Issue

Cite this: *RSC Adv.*, 2016, **6**, 62797

Hydroxyapatite doped CeO_2 nanoparticles: impact on biocompatibility and dye adsorption properties†

Savita Chaudhary,*[a] Priyanka Sharma,[b] Renu[a] and Rajeev Kumar[b]

The toxicity imparted by the commercialized use of nanoparticles in environmental remediation has become a big concern. To overcome this, the current work describes the fabrication of cerium oxide (CeO_2) containing hydroxyapatite (HAp) nanoparticles. The toxicity of the system was tested against the *Allium cepa* anaphase–telophase chromosome aberration assay. The enhanced stability and biocompatible nature of HAp widen the scope of engineered nanoproducts for wastewater treatment. Anionic Eriochrome Black T (EBT) dye was chosen as a model system for analyzing the adsorptive behavior of the engineered nanoparticles. The meticulous analysis of surface morphology, elemental composition, size and functional groups over the engineered product were ascertained by using microscopic and spectroscopic techniques. The corresponding influence of methodological aspects such as experimental pH, time, and concentration of the toxins and the nanoadsorbate toward the removal efficiency of pollutant were also quantified by using UV-Vis spectroscopic measurements. The kinetic and equilibrium adsorption analysis were also performed and a probable adsorption mechanism was determined for the prepared materials. The prepared HAp/CeO_2 nanohybrid can be exploited as a competent, low-cost adsorbent for the removal of dye molecules from the aqueous environment. This piece of work validates and promotes the idea of using biocompatible and non-toxic nanomaterials for environmental remediation, with high efficiency.

Received 16th March 2016
Accepted 11th June 2016

DOI: 10.1039/c6ra06933a

www.rsc.org/advances

1. Introduction

The last decade has witnessed a growing curiosity of researchers for developing smart, efficient and biocompatible nanomaterials with a diverse range of technological and industrial applications.[1–3] Out of various well-developed nanomaterials, cerium oxide (CeO_2) has generated significant interest in the scientific community.[4–7] CeO_2 nanoparticles have displayed unique functions as antioxidant and radioprotective agent in cancer therapy.[8] CeO_2 nanoparticles also have significant applications in chemical mechanical planarization, fuel catalysis, paints, *etc.*,[9] and play an important role as exogenous pro-resolving mediators in liver disease.[10] Additionally, CeO_2 nanoparticles have been used in developing anti-obesity pharmaceutical formulations.[11] Selvaraj *et al.*[12] have authenticated the role of CeO_2 nanoparticles in the prevention of lipopolysaccharide induced sepsis in male *Sprague Dawley* rats. The rising appreciation for these CeO_2 nanoparticles in industries has caused worry over their probable toxicity in the environment. In literature, there are several reports that specify the potentially lethal impacts of CeO_2 nanoparticles towards bacteria, fish, and mammalian cells.[13,14] The probable hazardous impact of CeO_2 nanoparticles to plants has also been investigated by different groups. For instance, Zhang *et al.*[15] have reported the effect of the accumulation of CeO_2 nanoparticles in the roots of cucumber (*Cucumis sativus* L.)

Therefore, for the safe use of CeO_2 nanoparticle based materials, caution must be exercised in determining the biocompatibility of these nanoparticles. In general, the biocompatibility of nanoparticles can be achieved by many methods, such as synthesizing nanoparticles from naturally biocompatible sources,[16] doping,[17] and coating the materials with biocompatible agents.[18–21] Due to the scarcity of the natural availability of biocompatible sources and the less usefulness of doped systems,[22,23] biocompatible coatings have an advantage in the synthesis of nanoparticles. The process of fabricating a biocompatible coating is comparatively easy and has minimum effects on the properties of the parent or core nanoparticles.[24] Out of various available biocompatible agents, calcium phosphate based compounds, such as hydroxyapatite (HAp), dicalcium phosphate (BCP), tricalcium phosphate (α and β-TCP), have gained significant attention from researchers, due to their extensive applications in the fields of materials science, medicine and biology.[25–27] Among these, HAp ($Ca_{10}(PO_4)_6(OH)_2$) has high stability in physiological conditions.[28,29] HAp is widely employed in orthopedic,[30] bone cementing,[27] and bone tissue

[a]*Department of Chemistry and Centre of Advanced Studies in Chemistry, Panjab University, Chandigarh 160014, India. E-mail: schaudhary@pu.ac.in; Fax: +91 172 2545074; Tel: +91 9417250377*

[b]*Department of Environment Studies, Panjab University, Chandigarh 160014, India*

† Electronic supplementary information (ESI) available. See DOI: 10.1039/c6ra06933a

engineering.[28] Currently, a composite coating of HAp over mesoporous silica nanoparticles has generated a significant role in drug delivery and also opposes unwanted bone resorption and speeds up fracture healing.[31]

The current work describes the fabrication of CeO_2 nanoparticles containing hydroxyapatite (HAp) nanoparticles in aqueous media. For the sake of comparison, the synthesis of the HAp–CeO_2 nanocomposite was also done in the presence of four different cationic surfactants and commercially available CeO_2 powder. The toxicity of all the studied systems was tested against the *Allium cepa* anaphase–telophase chromosome aberration assay. The seed germination experiments for wheat were also carried out to analyse the effect of nanoparticles on the growth inhibition rate. The enhanced stability and biocompatible nature of HAp widens the scope of CeO_2 nanoparticles for wastewater treatment. Anionic Eriochrome Black T (EBT) dye was chosen as a model system for analyzing the adsorptive behavior of CeO_2 nanoparticles. The meticulous analysis of surface morphology, elemental composition, size and functional groups were carried out by using microscopic and spectroscopic techniques. The as prepared nanohybrid acts as a competent, low-cost adsorbent for the adsorptive removal of dye from the aqueous environment with great efficiency.

2. Experimental

2.1. Materials

Cerium(III) nitrate hexahydrate (99%), cerium oxide powder (99.99%), calcium hydroxide (≥95.0%), *o*-phosphoric acid, CTAB (hexadecyl trimethyl ammonium bromide), CTAC (hexadecyl trimethyl ammonium chloride), CPB (cetyl pyridinium bromide hydrate 98%), CPC (cetyl pyridinium chloride), acetocarmine and mercury chloride were purchased from Sigma Aldrich. NH_4OH (ammonia solution, ~25%) was purchased from Merck. Absolute ethanol was obtained from Changshu Yangyuan Chemicals, China. Cationic Eriochrome Black T (EBT) was chosen as the adsorbate dye for evaluating the selective adsorption behavior over the as prepared nano hybrid of CeO_2/HAp. All the chemicals were used as purchased without any further purification. The standardization experiments were conducted using double distilled water, and real sample analysis was done on water collected from a hand pump; the Western Yamuna canal, Rohtak Division; tube well; tap and well water from Kiloi village, District Rohtak Haryana, India.

2.2. Synthesis of CeO_2 nanoparticles

2.2.1. Bare and surfactant-modified CeO_2 nanoparticles. Cerium nitrate hexahydrate was chosen as a starting material for the preparation of CeO_2 nanoparticles. In a typical experiment, 0.03 M cerium nitrate hexahydrate ($Ce(NO_3)_3 \cdot 6H_2O$) was dissolved in 50 ml of ethanol. About 25% aqueous solution of NH_4OH was added to the above solution in a drop-wise manner. The obtained mixture was aged for 24 hours. The resultant yellow dispersion was centrifuged and properly washed, dried and collected for further analysis. For preparing surfactant modified CeO_2 nanoparticles, the corresponding aqueous precipitation method was used.[32] The synthesis was similar to that explained for bare nanoparticles; the only difference was the addition of 0.03 M $Ce(NO_3)_3 \cdot 6H_2O$ in 0.05 M aqueous surfactant solution of CTAB, CTAC, CPC and CPB, followed by the addition of 1.3 M ethanol, and 0.25 M NH_4OH in 50 ml distilled water.

2.2.2. Impregnation of hydroxyapatite (HAp) nanoparticles over CeO_2 nanostructures. HAp loaded bare CeO_2 nanoparticles and surfactant functionalized CeO_2 nanoparticles were synthesized by the impregnation method. Briefly, a suspension of $Ca(OH)_2$ and CeO_2 nanoparticles (synthesized previously) was mixed in water under stirring conditions. The obtained suspension was subsequently heated to 80 °C under stirring. About 0.75 M of *o*-phosphoric acid (80%) was then added dropwise to the mixture. The obtained suspension was further kept under stirring for 2 h at 80 °C. The formed mixture contained HAp loaded CeO_2 nanoparticles. The resulting precipitates were separated from the solution by centrifugation and then washed with distilled water, followed by ethanol to removal all ionic impurities and then dried at 70 °C.

2.3. *Allium cepa* chromosome aberration assays

The presence of different types of chemical agents and nanoparticles has the ability to damage the chromosomal DNA of the living species. The variations further lead to genetic or mutagenic disorders in living organisms and lead to serious health hazards.[33] Therefore, the assessment of genotoxicity of the as prepared nanomaterials is essential for ensuring their use in environmental remediation, without causing damage to the biota.

In the current study, *Allium cepa* (onion) chromosomal aberration assay was used for analyzing the genotoxic effect of bare and functionalized CeO_2 nanoparticles. For the sake of comparison of toxicity generated by bulk and nanometric particles, trials with commercial CeO_2 powder have also been carried out. For experimentation, onion bulbs were cultivated without the application of any external herbicides or fungicides in the growing media. The bulbs were scraped from the root to facilitate the emergence of new roots. To obtain the rootlets, the onions were allowed to grow in 100 ml solutions containing 100 ppm of different types of nanoparticles and CeO_2 powder for 3–4 days, or until 2–3 cm rootlets emerged. Water was used as a negative control in the subsequent analysis. In order to exclude the effect of onion quality, 5 groups of *Allium cepa* were used for each treatment of the as fabricated nanoparticles.

The representative roots of 1 cm length were cut by using sterilized scissors, and transferred to a plastic microtube containing 1 N HCl. The resultant was then incubated at 60 °C for 12 minutes over a water bath. The obtained roots were then carefully transferred to a Petri dish and washed with distilled water. The root tips were stained with acetocarmine dye for the specific visualization of chromosomal aberrations in *Allium cepa*. Slides were prepared by cutting the stained root tip over glass slides. The cover slip was gently placed over the slide and tapped to spread the cells and viewed under an electron

microscope. The corresponding value of mitotic index (MI) was calculated according to following equation:

$$\mathrm{MI} = \frac{\mathrm{P} + \mathrm{M} + \mathrm{A} + \mathrm{T}}{\text{total number of cells in the interphase}} \quad (1)$$

where P + M + A + T = total number of cells in Prophase, Metaphase, Anaphase and Telophase, respectively. The relative mitotic index (RMI) and the chromosomal aberration index (CAI) were also calculated in accordance with eqn (2) and (3):

$$\mathrm{RMI} = \frac{\mathrm{MI}}{\mathrm{MI_C}} \quad (2)$$

where MI is the mitotic index for each treatment and MI_C is the MI value of the control process.

$$\mathrm{CAI} = \frac{\mathrm{CA}}{\mathrm{TD}} \times 100 \quad (3)$$

where CA is the number of divisions with chromosomal aberrations and TD is the total number of divisions. All the calculations were made for 5 groups and the average values were taken with respective standard deviations.

2.4. Seed germination bioassay

The inhibitory effect of CeO_2 nanoparticles and commercially available CeO_2 powder on wheat seed germination has been used to monitor the cytotoxic and anti-proliferative effects in the presence of nanoparticles. The main objective of this study is to provide an alternative to the animal or human bioassay model.[34] The presence of nuclei in plants makes them comparable to animal and human cells; as a result, the variations in the biochemical expression of plants in the presence of different analytes can be correlated, to a great extent, with animals as well as humans beings.

2.4.1. Experiment plant (*Triticum aestivum*). Best quality wheat (*Triticum aestivum*) seeds of uniform weight (55 ± 4 mg), were purchased from the grain market in Chandigarh, India. The seeds were subjected to viability testing by submerging them in water and the floating seeds were discarded. The submerged seeds were dried and then sterilized with 0.1% mercuric chloride solution for 5 minutes, followed by 5–6 washings with distilled water.

The as dried seeds were soaked in 30 ml of distilled water for the control, and in an aqueous solution of nanoparticles and CeO_2 powder for 48 h. The seeds were then transferred to Petri dishes with their respective solutions. The seeds were allowed to grow for 4 days under dark and warm conditions. The sprout length was measured with thread. All experiments were carried out in triplicate and the average was taken for further calculations. The obtained results were expressed in terms of percentage inhibition growth (PIG).

$$\mathrm{PIG} = \left[\frac{\mathrm{LC} - \mathrm{LN}}{\mathrm{LC}}\right] \times 100 \quad (4)$$

where, LC is the average length in the control and LN is the average length in the nanoparticles solution.

3. Characterizations

The optical properties of the as-prepared nanoparticles were analyzed by using a LABINDIA UV-Vis spectrophotometer. The fluorescence analysis was done by using a Hitachi F-7000 spectrophotometer. The crystallographic structural analysis was carried out on a Panalytical D/Max-2500 powder diffractometer with monochromatic CuKα radiation (λ = 1.5406 Å) over the 2θ range of 5–90° at a scan rate of 2 deg min^{-1}. The operational voltage and the currents were 40 kV and 30 mA, respectively. Fourier transform infrared (FT-IR) spectroscopy (Perkin-Elmer (RX1)) was used to identify the functional groups in the working range of 4000–400 cm^{-1}, with 2 cm^{-1} resolution, averaging 100 scans. The morphological analysis was carried out by TEM (Hitachi (H-7500)) and SEM (Hitachi (SU8010)) analysis. The measurements of particle size (90° optics) and zeta potential studies were done on a Nano S 90 ((Red badge), Malvern Instruments Corporation, model no. ZEN 1690). The thermal analysis of the as-prepared nanoparticles was done with a TG–DTG (thermogravimetric analysis) on SDT Q-600, from TA Instruments. The surface area of the as prepared nanoparticles was estimated by using BET analysis with N_2 adsorption analyzer (NOVA 2000e) USA. Chromosomal aberration experiments were carried out using a Nikon Eclipse E-200 light microscope with an attached camera. The images were visualized and captured at 100× magnification by using acetocarmine stain. The loading of the EBT dye molecules over the nanoparticles in adsorption experiments were analyzed by elemental mapping through SEM analysis.

4. Results and discussion

4.1. Structural characterization

In the current work, hydroxyapatite (HAp) was chosen as a safe alternative for synthesizing biocompatible CeO_2 nanoparticles in aqueous media. The structural evolution of the as obtained particles was carried out by a series of experiments. The resultant morphologies of pure HAp and HAp–CeO_2 were investigated by SEM and TEM analysis (Fig. 1).

The pure HAp nanoparticles show irregular, rod-like structures with length of around 50–100 nm. In the presence of CeO_2, the particles appeared to be less distorted and the obtained size was lower than that of the pure HAp nanoparticles. The bare CeO_2 nanoparticles also show the higher rate of agglomeration. The obtained values for aggregation size of bare CeO_2, pure HAp and HAp coated nanoparticles were 80 nm, 96 nm and 76 nm, respectively. The obtained surface area for bare CeO_2, pure HAp and HAp coated nanoparticles were 9.15 m^2 g^{-1}, 6.03 m^2 g^{-1} and 7.65 m^2 g^{-1}, respectively. The respective elemental mapping of HAp coated CeO_2 nanoparticles are shown in Fig. 2. The irregularity in pure HAp was associated with the quick interaction of freely available Ca^{2+} ions with PO_4^{3-} ions. This leads to a higher precipitation rate of HAp in reaction media. On the other hand, in the presence of CeO_2 nanoparticles, the corresponding rate of interaction between the two ions was decreased and led to the confined growth of HAp nanoparticles.

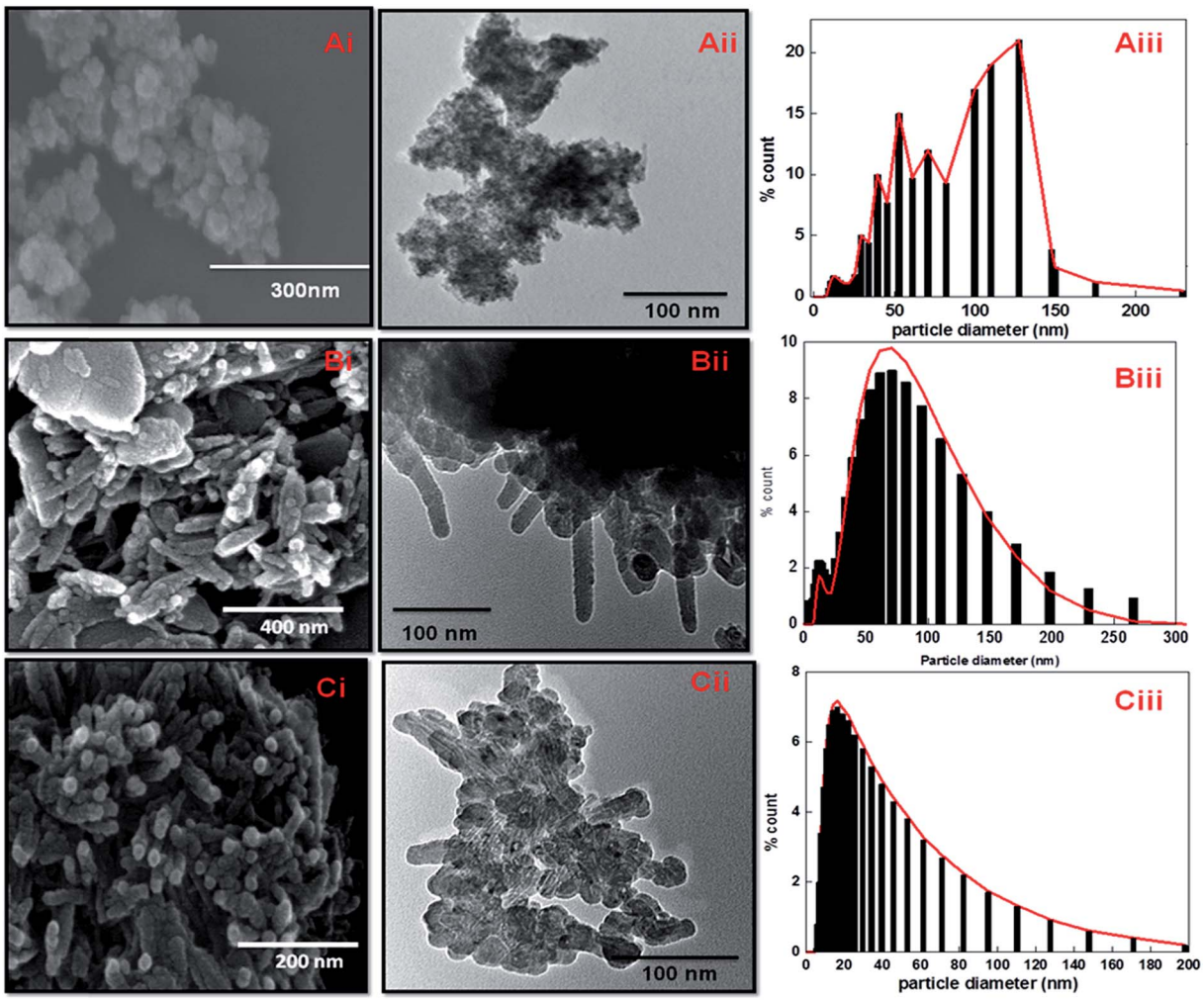

Fig. 1 FESEM, TEM and particle size distribution of (Ai–Aiii) bare CeO_2, (Bi–Biii) pure HAp and (Ci–Ciii) HAp coated CeO_2 nanoparticles.

The shape of the obtained nanoparticles was further reformed in the presence of HAp nanoparticles over surfactant capped CeO_2 nanoparticles (Fig. 3). The surfactant chosen was cationic in nature, which enhances the adsorption of negatively charged dye used in this work. The four types of surfactants used in this work have the same chain length, but differ in the counterions, as well as the head groups of the surfactant. Therefore, the current work gives the detailed comparison of the effect of surface coating on the dye removal efficiency in the presence and absence of HAp. Moreover, the presence of surfactant template also influenced the interaction rate of Ca^{2+} ions with PO_4^{3-} ions.

The rod-shaped particles were less abundant in the presence of surfactant capped CeO_2 nanoparticles. The sharp multiple fiber-like morphology was obtained from the central point in the case of HAp coated CTAB functionalized CeO_2 nanoparticles (Fig. 3Ai). The corresponding length of such structures varied at around 500 nm with the corresponding width of less than 20 nm. The close inspection of the TEM image (Fig. 3Aii) showed the presence of two well-defined types of particles. One depicted the presence of small sized CeO_2 nanoparticles (dark contrast) over the surface of HAp nanoparticles (low contrast); the variations were associated with the directional growth of HAp in the presence of functionalized nanoparticles. However, in the case of CTAC, CPC and CPB functionalized CeO_2 nanoparticles, there was the abundance of more spherical particles. The obtained particles showed more uniformity in the structures. These behavioral changes are mainly associated with the selective growth of nanoparticles along the preferential crystallographic direction in the presence of surfactants.[32] The corresponding particle diameter frequency distribution plots for HAp–CeO_2 nanoparticles in the presence of surfactants are shown in Fig. S1 (ESI†). The EDS elemental analysis was also carried out to check the purity and stoichiometry of the formed nanoparticles (Fig. S2 (ESI†)).

The corresponding changes in the morphological structures were further investigated through FTIR analysis (Fig. 4). The pure HAp nanoparticles show the characteristic peaks of the phosphate group. The asymmetric stretching peak for the P–O band was observed at 1066 cm^{-1}. The respective O–P–O, P–H and P=O bands appeared between 560 and 500, 2340 and 1140 cm^{-1}. The hydroxyl band was evident at 3400 cm^{-1}. The

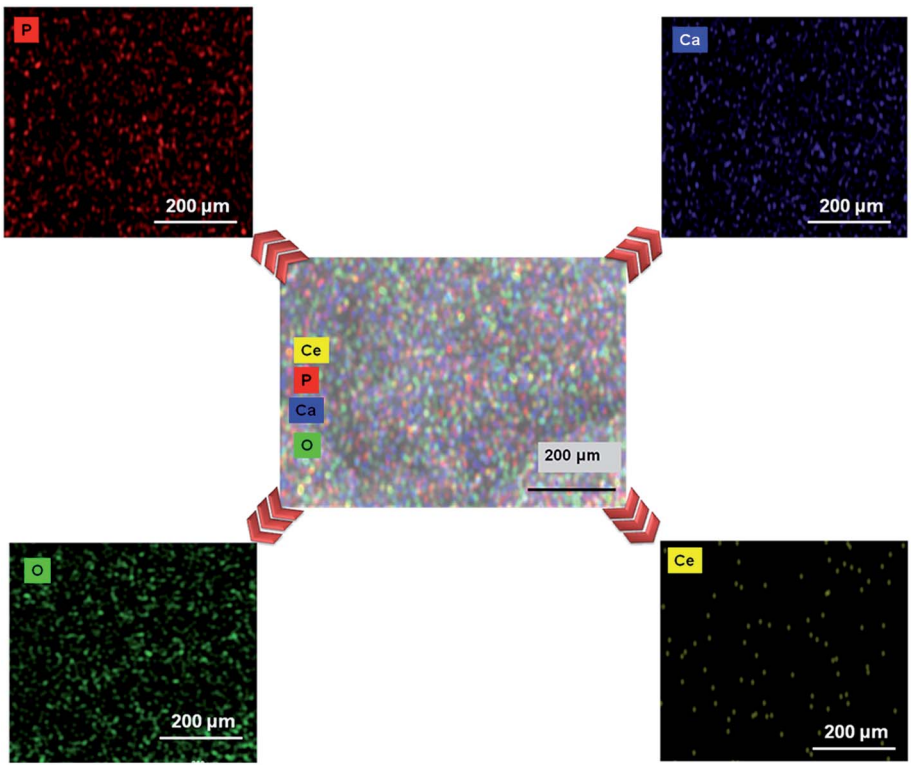

Fig. 2 The elemental mapping of HAp coated CeO_2 nanoparticles, showing the individual and combined presence of Ce, O, P and Ca atoms in the system.

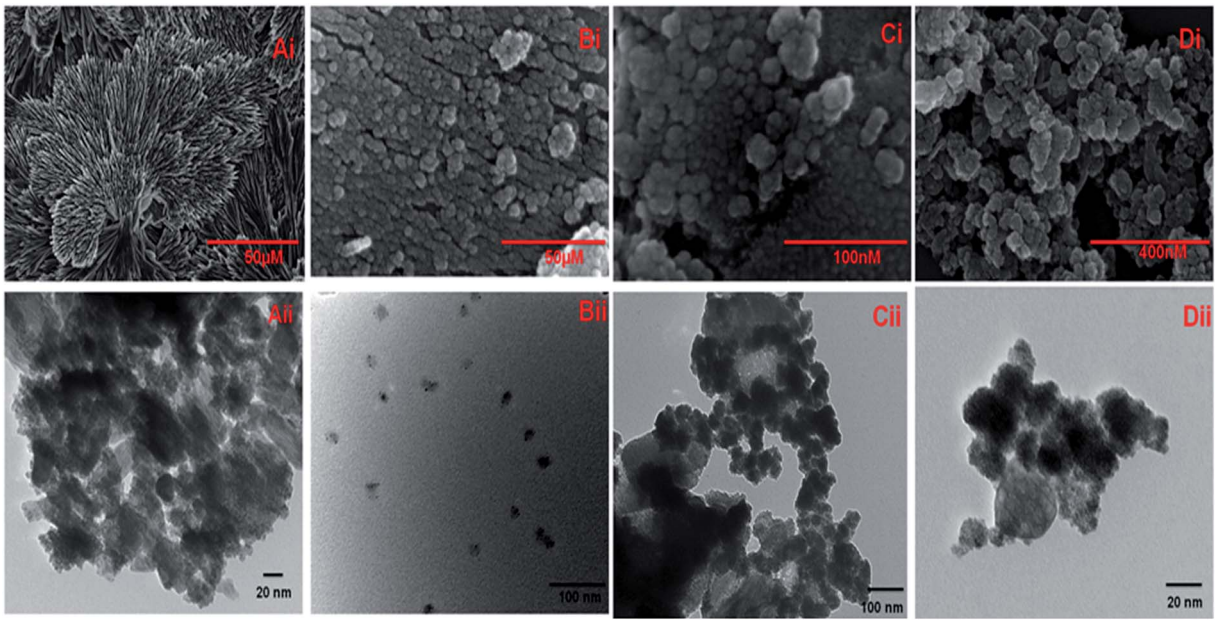

Fig. 3 The corresponding FESEM and TEM images of (Ai and Aii) CTAB, (Bi and Bii) CTAC, (Ci and Cii) CPB and (Di and Dii) CPC functionalized CeO_2 nanoparticles in the presence of HAp.

absorption peak below 700 cm^{-1} corresponds to the Ce–O peaks in the case of HAp–CeO_2 nanoparticles.[32] The P–O band appeared at 1072 cm^{-1} in the presence of CeO_2, and was also blue shifted by 13 cm^{-1}. The marked differences are detected between 600 and 400 cm^{-1} in the presence of bare and surfactant functionalized CeO_2 nanoparticles. The intensities of the peaks at 558 and 520 cm^{-1} also show variations. Such changes are associated with the difference in the crystalline growth of HAp nanoparticles in different reaction media.

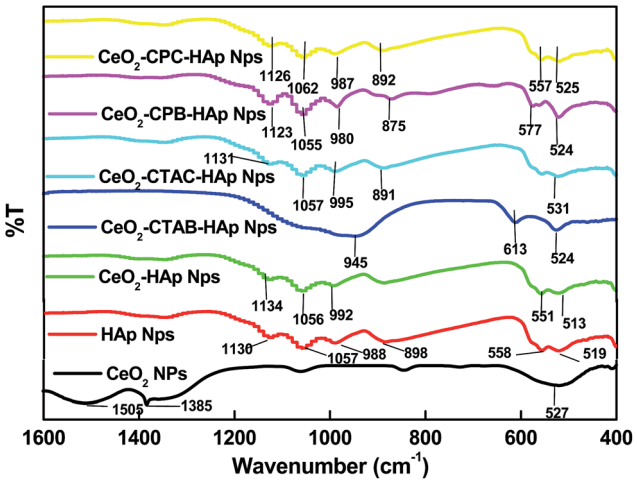

Fig. 4 FTIR spectra of HAp nanoparticles synthesized in the absence and presence of bare and surfactant functionalized CeO_2 nanoparticles.

In order to determine the growth mechanism of HAp in the presence of CeO_2 nanoparticles, the respective phase analysis of particles was conducted using the XRD studies. Fig. 5 shows the typical XRD profile for the as obtained nanoparticles. The strong intense peaks at $2\theta = 26.67°$, 30.36°, 32.05°, 32.86° and 33.05° correspond to the ⟨002⟩, ⟨211⟩, ⟨112⟩, ⟨300⟩ and ⟨202⟩ planes of the crystalline structure for bare HAp nanoparticles.[34] The obtained results were comparable to the database of the Joint Committee on Powder Diffraction Standards (JCPDS) card number: 9-432. The XRD spectra of bare CeO_2 nanoparticles displayed characteristic peaks at 28.4° and 47.5°. On another hand, the XRD profiles of HAp coated CeO_2 nanoparticles in the presence and absence of surfactants show relatively broader peaks. The intensities of the peaks also show significant variations in the presence of surfactant modified CeO_2 nanoparticles. The corresponding comparison for the peak intensities of 3 planes, *i.e.* ⟨002⟩, ⟨211⟩ and ⟨112⟩ have been tabulated in Table S1 (ESI†). An estimation related to the crystallite size for nanoparticles, according to Scherrer's formula[35,36] further reveals a proportional increase in the crystallite size of pure HAp nanoparticles, as compared to HAp coated CeO_2 nanoparticles, in the presence and absence of surfactants (Table S1†).

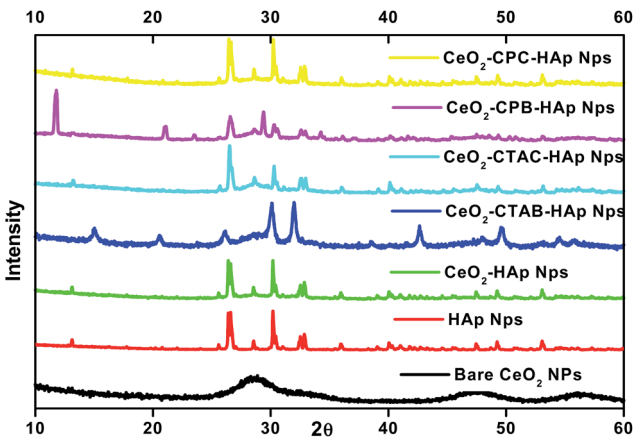

Fig. 5 XRD spectra of pure HAp nanoparticles, HAp coated CeO_2 nanoparticles, HAp coated CTAB–CeO_2 nanoparticles, HAp coated CTAC–CeO_2 nanoparticles, HAp coated CPB–CeO_2 nanoparticles and HAp coated CPC–CeO_2 nanoparticles.

From the data, it has been anticipated that the intensity ratio of the peaks at the ⟨211⟩ and ⟨002⟩ planes was more in the case of HAp coated CTAB and CPB functionalized CeO_2 nanoparticles. This variation explained the greater crystalline growth of HAp in the ⟨211⟩ plane, as compared to the ⟨002⟩ plane. On the other hand, pure HAp, HAp coated CeO_2 in the absence of surfactants, and in the presence of CPC, show equivalence in intensity ratio. The results were interpreted *via* the slower diffusion of PO_4^{3-} ions in the presence of surfactants; the presence of surfactants over the surface of CeO_2 nanoparticles acts as a hindrance barrier for the PO_4^{3-} and Ca^{2+} ions. The presence of surfactants in the reaction media further lowers the addition rate of PO_4^{3-} ions over the Ca^{2+} ions. This decrease in diffusion rate enhances the crystalline growth of nanoparticles in a preferential direction. The presence of N^+ charge in the head group of surfactants causes the formation of bonds with PO_4^{3-} ions. Such electrostatic interactions provided the additional alignment of growing nanoparticles along the specified axis during crystal growth of HAp in the presence of surfactants. The corresponding ε (strain), σ (stress) and μ (energy density) for the as functionalized nanoparticles have also been calculated by using well defined Williamson–Hall methods.[37] The used value of Young's modulus of elasticity was taken as 3.9 GPa for the current study.[38] The obtained results are tabulated in Table S1 (ESI†). Fig. S3† has shown the comparative thermal gravimetric analysis for pure HAp, CeO_2 and CeO_2 impregnated HAp nanoparticles. In the spectra, the small weight losses up to 200 °C correspond to the evaporation of residual water or moisture from the as formed nanoparticles. In the case of pure HAp nanoparticles, the first 10% weight loss was associated with the dehydration of HPO_4^{2-} ions to $P_2O_7^{2-}$ ions; whereas, surfactant modified CeO_2 in the absence and presence of HAp possess two main weight losses in the temperature range of 300–500 °C. These losses were associated with the exclusion of surfactant templates, followed by the HAp layer from the exterior surface of CeO_2 nanoparticles. The optical and luminescence properties of as-synthesized nanoparticles were also analyzed using UV-Vis and fluorescence studies (Fig. S4, ESI†). The photoluminescence (PL) spectrum of the as-synthesized nanoparticles was measured by exciting the samples with $\lambda =$ 290 nm (Fig. S4a†). All the water dispersed solutions containing CeO_2 nanoparticles have shown a blue emission peak in the range of 350 to 410 nm. These peaks were attributed to the surface defects and dislocations, which are helpful for fast oxygen transportation in CeO_2 nanoparticles.[32] In the case of pure HAp, no such peak was visible in this range. In the presence of HAp over CeO_2 nanoparticles, there was reduced luminescence intensity for this peak. The intensity variation over this peak in the presence of HAp with CeO_2 was related to the suppression of surface defects of CeO_2. These results were further verified by carrying out the UV-Vis analysis of as

prepared samples in the presence and absence of HAp (Fig. S4b†). These shifts in the peaks were mainly associated with the suppression of surface defects of CeO_2. Moreover, the size variation was also responsible for the changes in the peak positions of the UV-Vis spectra.

4.2. *Allium cepa* chromosome aberration assays

The genotoxic and mutagenic effects of harmful toxins have also been determined from their damaging impact on the DNA. From the literature, it is quite evident that nanoparticles have the tendency to trigger free radical formation in cells.[39] The small size of the particles support their diffusion inside the cell wall, or these particles can be actively taken up by phagocytosis.[40] The formation of reactive oxygen species, which are mainly responsible for the disruption of cell function, was mainly dependent on the particle size and structure. In the current work, genotoxic studies of the as formed nanoparticles and commercially available CeO_2 powder (1000 ppm) were carried out by using *Allium cepa*. Fig. 6a and b show the results of the different percentages of cells in the prophase, metaphase, anaphase and telophase of *Allium cepa* after treating it with different nano formulations. The corresponding results of % mitotic index and % relative mitotic index values are presented in Fig. 6c and d in the presence and absence of HAp. The respective chromosomal aberration index values are presented in Table S2 (ESI†). The chromosome aberration indices were absent in the case of control bulbs (Fig. 7). The observed mitotic index value for the blank was 80.36%. On the other hand, bare CeO_2 nanoparticles showed an increased number of aberrations with a mitotic index value of 18.5% (Fig. 8).

The chromosome aberration indices were also evident in the presence of surfactant capping over the CeO_2 nanoparticles. The respective MI values varied between 16.8 and 21.8% (Fig. 6c) for surfactant functionalized CeO_2 nanoparticles. Alternatively, the nano formulations containing HAp at low concentrations generated less chromosomal aberrations, compared to bare and surfactant coated CeO_2, signifying that the association of the biocompatible nanoparticles with the system was able to reduce the harm to the DNA of the *Allium cepa* cells. However, the coating of HAp over bare CeO_2

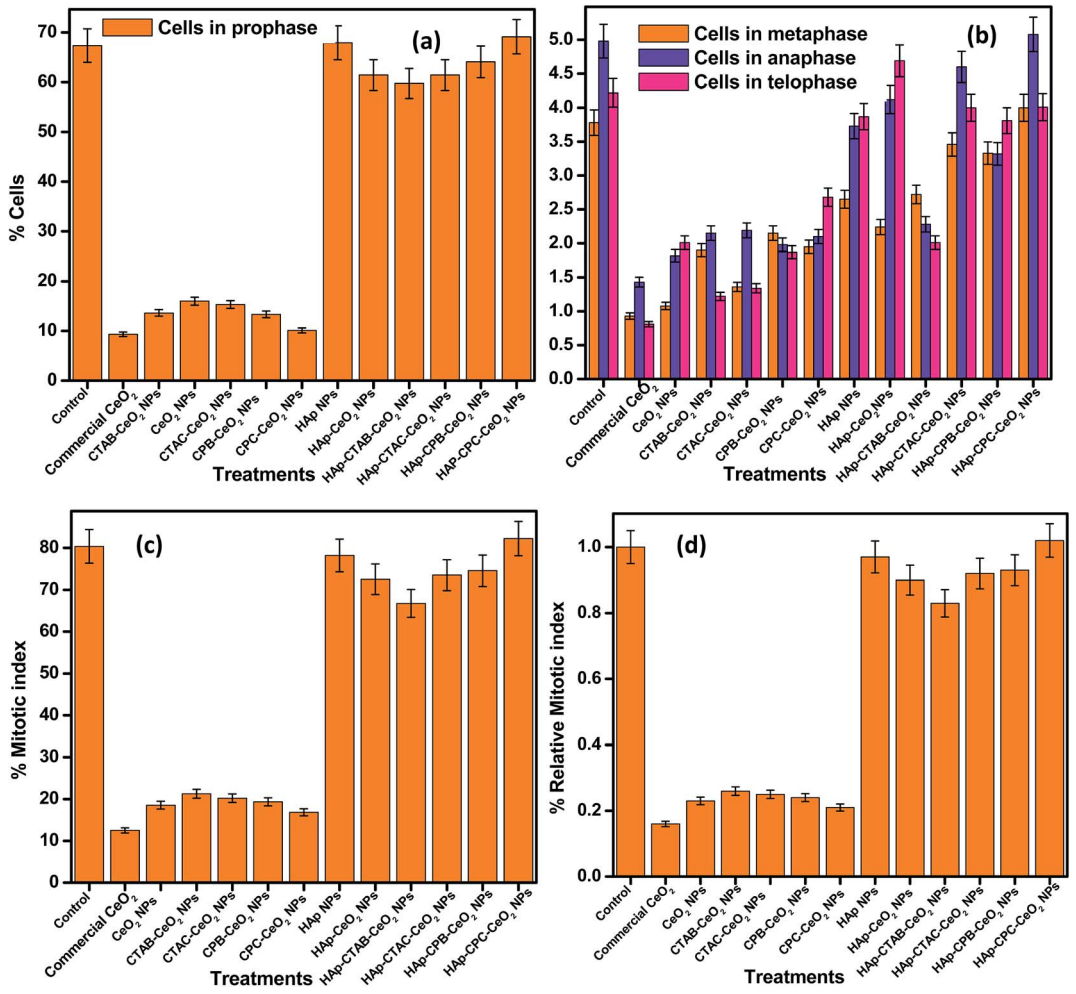

Fig. 6 The variation of percentage cell values as a function of (a) cells in prophase, (b) cells in metaphase, anaphase, telophase (c) percentage mitotic index and (d) relative mitotic index for control, pure HAp and bare and surface functionalized CeO_2 nanoparticles in the absence and presence of HAp coating, with concentration equivalent to 1000 ppm.

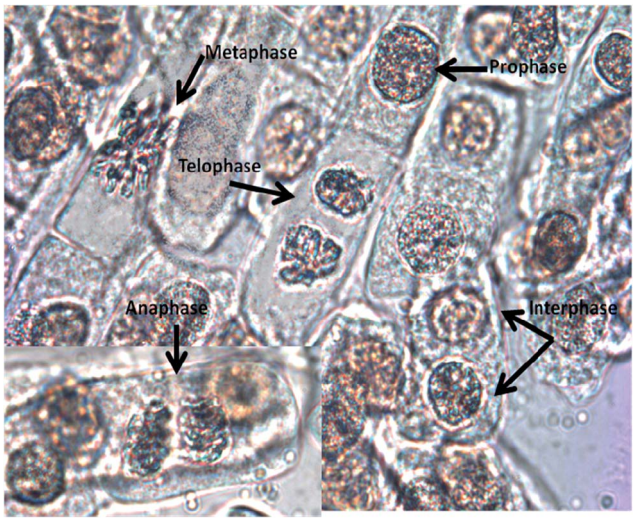

Fig. 7 Different stages of mitotic division such as interphase, prophase, metaphase, anaphase and telophase in control treatment.

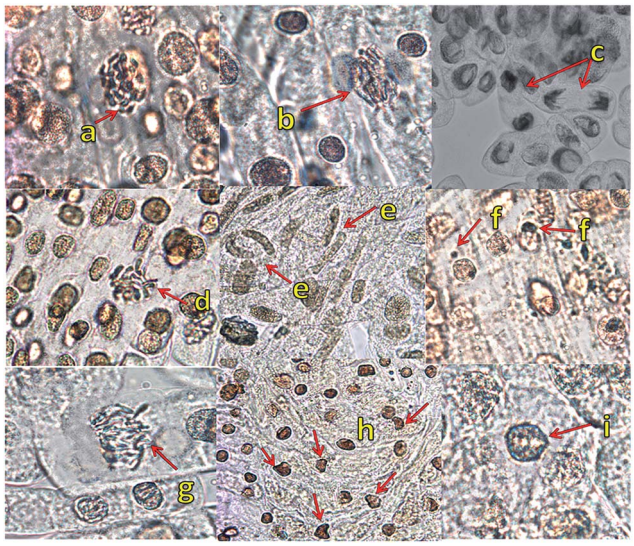

Fig. 8 Chromosomal aberrations observed in *Allium cepa* root tips in the presence of CeO_2 nanoparticles (a) clumped chromosomes, (b) anaphase bridge, (c) disturbed anaphase, (d) sticky chromosomes, (e) laggard chromosomes, (f) micronuclei formation, (g) disturbed metaphase (h) nuclear notch and (i) binucleate cell.

nanoparticles also displayed less chromosomal aberrations with MI values of 72.5%, as compared to the 18.5% for bare CeO_2 in absence of HAp. The MI values of surfactant functionalized CeO_2 nanoparticles have also shown significant improvement in the presence of HAp. The CeO_2 nanoparticles have a smaller size, compared to HAp doped CeO_2 nanoparticles, which leads to the larger production of ROS by the undoped CeO_2 nanoparticles.[40] Due to the larger surface area to mass ratio of smaller particles, more ROS is formed.[41] The HAp grafting over the CeO_2 nanoparticles surface blocks the nanoparticle surface–cytosol interaction and creates a steric barrier. Also, the biomimetic nature of HAp avoids the interruption of redox homeostasis of the cell by HAp doped CeO_2 nanoparticles, thus reducing its genotoxicity. The highest toxicity imparted by bulk CeO_2 powder could be related to the extra damage caused to cells, due to the irregular shape and huge size of the particles. These particles could also block the cell wall channels and inhibit the proper functioning and proliferation of the cells. The results clearly indicate the utilities of developed HAp formulations with minimum damage to the environment.

4.3. Seed germination assay

The antiproliferative activity of the as formed nanoparticles with 1000 ppm concentration showed higher PIG values, ranging from 96.16 to 100% (Fig. 9 and Table S3†), whereas, at the same concentration the HAp coated nanoparticles showed 0.00 to 7.7% PIG. These results have clearly indicated that there was a huge difference in the antiproliferative activity of CeO_2 nanoparticles in the absence and presence of HAp coating. The reason could be assigned to the biocompatible nature of HAp and the size enhancement with HAp coating over the surface of nanoparticles (Fig. S5†).

4.4. Adsorption studies

The characteristic properties of nano-adsorbents, including the nature of functionalization, size and their interaction efficacy with the adsorbates, are the principal factors that govern the adsorptive removal efficiency of the system.[32b] The HAp functionalized CeO_2 nanoparticles in the absence and presence of surfactants have also been tested for their sorption capacity against Eriochrome Black T (EBT) dye as a model system in this work. The adsorption of dye molecules has been achieved *via* the electrostatic interactions between the surface functionalized nanoparticles and dye molecules. The presence of surfactants over the surface of nanoparticles has further enhanced the adsorption efficiency of the nanoparticles by modulating their size and also through aromatic interactions between the head groups of surfactants and hydrophobic dye molecules. The batch experiments for the adsorptive removal of Eriochrome Black T (EBT) from its aqueous solution were conducted with all

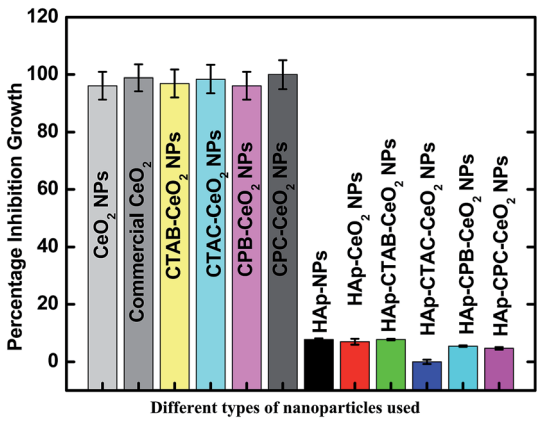

Fig. 9 The percentage inhibition growth of *Triticum aestivum* in the presence of different nanoparticles.

the prepared nano-formulations. The optimization of the data was done by elucidating the influence of different parameters, including nanoparticle dosage amount, initial dye concentration, pH and contact time for all the respective systems. The digital imaging of HAp–CTAB coated CeO_2 nanoparticles as a function of pH, nanoparticles dosage amount and contact time is shown in Fig. S6 (ESI†).

4.4.1. Influence of pH. The chemical interactions of dye in nano-formulations and the respective ionization behavior of sorbate (dye) and sorbents are influenced by the pH of the reaction media. The zeta potential measurements for the as synthesized nanoparticles were also done to find the exact mechanism of dye adsorption over the nanoparticles. For this purpose, 5 mg of each type of nanoparticles were dispersed in 5 ml of buffer solution using an ultrasonic bath. Afterwards the nanoparticles were centrifuged and redispersed in 5 ml of triply distilled water. Different pH values of 2, 4, 6, 7, 8, 10 and 12 were maintained using 1 N HCl and 1 N NaOH. At low pH values, the nanoparticles possess positive values of zeta potential, due to the adsorption of H^+ ions from aqueous media. At high pH values, the surface of the nanoparticles has the tendency to adsorb OH^- ion and possess negative zeta potential values. Fig. S7† shows the variation of zeta potential values as a function of pH for different types of nanoparticles under study. For bare CeO_2 nanoparticles, the pH_{PZC} (zero point charge value) lies between 6.37 and 6.56, whereas, HAp functionalized nanoparticles have pH_{PZC} at ~6.46 to 6.6. This similarity in pH_{PZC} with and without functionalization enabled us to carry out adsorption studies for all these nanoparticles at the same pH value (Table S4†). Therefore, in the current study, the working pH for EBT adsorption was taken as 5. In the case of surfactant coating along with HAp functionalization, there was a higher value of pH_{PZC}. This behavioral variation was the main reason for the higher adsorption efficiency of EBT dye over surfactant-coated nanoparticles at low pH values.

The adsorption efficiency of EBT on different nano formulations was tested as a function of pH variations. The adsorption batches were carried with 50 ppm of EBT dye in 50 ppm concentration of nanoparticles in the pH range from 2–12 at room temperature (Fig. 10a). The corresponding effect of bare CeO_2 nanoparticles as a function of pH is included in Fig. S8.† The supernatant and solid residues were separated by centrifugation at 4000 rpm for 10 min. The concentration of the dye was investigated by measuring the absorption value at λ_{max} = 520 nm.

The percentage removal of EBT dye was calculated by using the following relationship:

$$\text{Percentage removal} = \frac{C_o - C_t}{C_o} \times 100 \quad (5)$$

where C_o is the initial concentration of dye in ppm and C_t is the equilibrium sorbate concentration. From Fig. 10a, it is evident that the uptake of EBT decreased as the pH of the solution increased in the reaction media. The behavioral changes were associated with protonation of the phosphate groups present over the surface of the HAp coated nanoparticles in acidic media (pH = 2–5). The as prepared $H_2PO_4^-$ ions further facilitated the binding of anionic EBT dye with nanoparticles. On further increasing the pH from 6 to 7, the formation efficiency of HPO_4^{2-} was affected, which further contributed to the decrease in the adsorptive removal of dye molecules from

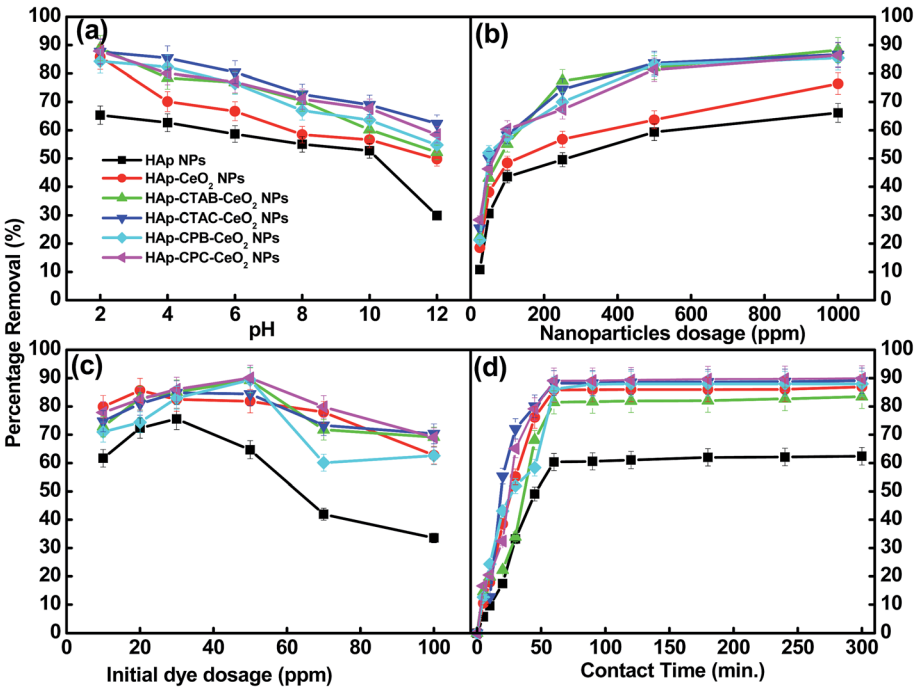

Fig. 10 Effects of different parameters on the dye removal efficiency of pure HAp and bare and surface functionalized CeO_2 nanoparticles in the absence and presence of HAP coating: (a) pH, (b) nanoparticles dosage, (c) initial dye dosage and (d) contact time.

aqueous media. On further increasing the pH to 12, the deprotonated form of the phosphate group *i.e.* PO_4^{3-} was formed, which showed highly repulsive behavior towards the anionic dye, EBT. These results further suggested that the maximum adsorptive removal efficiency of EBT was achieved at pH = 5, and this pH was further employed to optimize other parameters for dye removal applications.

4.4.2. Influence of adsorbent dosage. The respective amount of sorbent employed to remove dye molecules from its per unit volume solution is a significant parameter to check the economics of the prepared method.[32b] The corresponding plots of adsorptive removal efficiency *vs.* adsorbent dosages at room temperature for different nanoformulations are presented in Fig. 10b with fixed dye concentration of 50 ppm at pH = 5. As evident for the fixed concentration of dyes, the adsorption capacity varied linearly with the amount of adsorbate added in the reaction system. These results were explained on the basis of higher available surface area and respective enhanced adsorption sites for the removal of dye molecules.

4.4.3. Effect of initial dye concentration. The effect of different initial dye dosages (*i.e.* 10, 20, 30, 50, 70 and 100 ppm) was also tested against the nanoparticle dosage amount of 50 ppm at pH = 5 for all the prepared nanoparticles (Fig. 10c). The percentage removal efficiency of EBT increased with increase in EBT concentration until a saturation point of 50 ppm was attained. Beyond this concentration, the percentage removal of EBT decreased due to the unavailability of vacant adsorption sites over the surface of the nanoparticles.

4.4.4. Effect of contact time. The corresponding influence of the adsorptive removal efficiency of EBT dye over the surface of the nanoparticles was also tested as a function of contact time (Fig. 10d) in the presence of 100 ppm of nanoparticles and 50 ppm EBT dye at pH = 5. As evident from the results, the removal efficiency of the dye shows a linear increase with increasing contact time. The distinct increasing percentage removal efficiency occurred up to 60 min and attained constancy after 1 hour. These findings further confirmed that a minimum contact time of 60 minutes was sufficient to effectively remove more than 95% dye from its aqueous media.

4.5. Adsorption isotherms

The respective interactional behavior of dye molecules with nanoparticles at a given temperature under equilibrium conditions was further investigated by isothermal analysis.

The equilibrium adsorption data of the EBT dye was analyzed by applying the well acknowledged Langmuir and Freundlich model. The linearized form of the Langmuir isotherm is expressed as follows:

$$\frac{C_e}{q_e} = \frac{1}{bq_{max}} + \frac{1}{q_{max}}C_e \quad (6)$$

where C_e is the equilibrium concentration of dye, q_e the amount of dye adsorbed (mol g^{-1}), q_{max} and b are Langmuir constants related to the adsorption capacity (mol g^{-1}) and energy (L mol^{-1}), respectively (Fig. S9†). The Langmuir model assumes the monolayer adsorption of dye molecules (*i.e.* one molecule thick adsorbed layer) at a fixed number of localized sites over nanoparticles. This model has also assumed that no lateral interaction and hindrance between the adsorbed molecules occurred with adjacent sites over adsorbate. The obtained values of q_{max} and R^2 for different nanoparticles are tabulated in Table S5.† On the other hand, the Freundlich equation was based on a heterogeneous surface:

$$\log q_e = \log Q_f + \frac{1}{n}\log C_e \quad (7)$$

where Q_f and n are empirical constants and their values are obtained by plotting $\log q_e$ *vs.* C_e. The value of the $\log Q_f$ is obtained from the intercept and n is the slope of linear fitting (Fig. S10†). The assessment of estimated coefficients (R^2) of EBT indicates that adsorption over HAp in the absence and the presence of CeO_2 nanoparticles can be better explained by the Freundlich isotherm equation, which suggests the multilayer formation of dyes over the surface of the nanoparticles. In addition, the higher values of n greater then unity further support the interaction of dye molecules with surface nanoparticles. The elemental mapping of dye-coated HAp impregnated CTAC–CeO_2 nanoparticles has also confirmed the surface adsorption of EBT dye over the surface of the nanoparticles

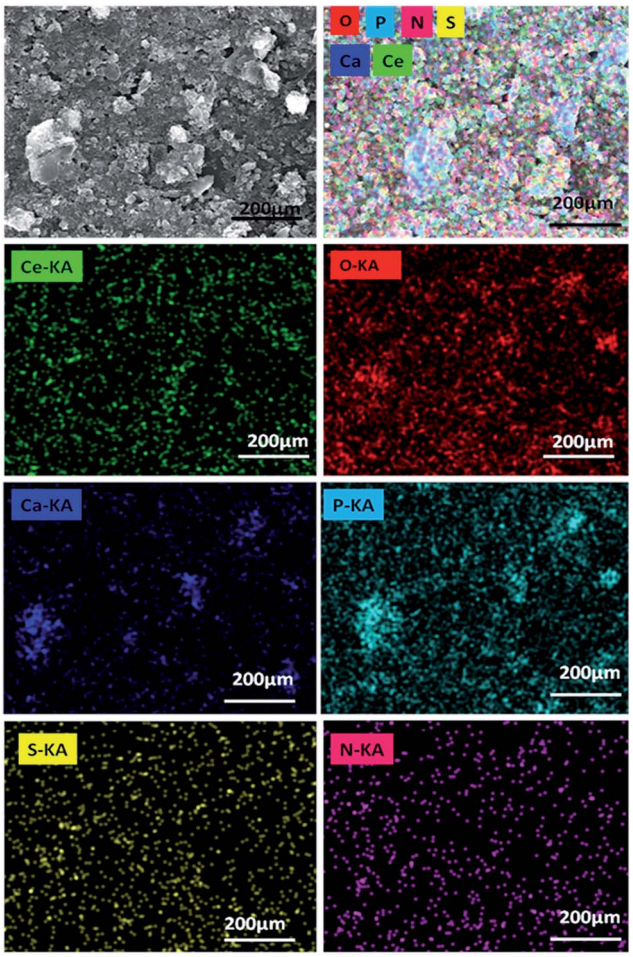

Fig. 11 Elemental mapping of dye adsorbed CTAC functionalized CeO_2 in the presence of HAp nanoparticles.

Table 1 Adsorption kinetics models of EBT dye on all nanoparticles

	Pseudo first order		Pseudo second order		
Nanoparticles	K_1	R^2	K_2	q_e	R^2
HAp	0.045	0.99	88.49	0.767	0.90
CeO_2–Hap	0.033	0.99	155.76	1.055	0.96
CTAB–CeO_2–HAp	0.189	0.96	89.85	1.119	0.98
CTAC–CeO_2–HAp	0.038	0.99	50.23	4.619	0.98
CPB–CeO_2–HAp	0.218	0.95	73.26	1.391	0.94
CPC–CeO_2–HAp	0.037	0.99	57.94	3.186	0.98

(Fig. 11). Single element mapping of Ce and O has shown the small sized CeO_2 nanoparticles; the appearance of Ca and P in agglomerated and large sized particles confirms the encapsulation of CeO_2 nanoparticles by HAp. The abundance of the pink color that is formed due to the collective effect of S (yellow) and N (purple) is proof of the surface adsorption of EBT dye on HAp–CTAC–CeO_2 nanoparticles. Similar results were obtained for other synthesized nanoparticles (results not shown here).

4.6. Adsorption kinetics

In order to examine the controlling mechanism of the adsorption processes, such as mass transfer and chemical reaction, pseudo first and second-order kinetics were used to test the experimental data. The pseudo first-order chemisorption kinetic rate equation is expressed as follows:

$$\ln\frac{C_o}{C_e} = K_1 t \quad (8)$$

where C_o and C_e are the initial and equilibrium concentrations of EBT in the solution and K_1 is the rate constant (min^{-1}). The values for rate constant K_1 and regression coefficient R^2 have been calculated from the plot of $\ln C_o/C_e$ *vs.* t (Fig. S11a†) and are tabulated in Table 1. The linear form of the pseudo second order kinetic model is expressed as follows:

$$\frac{t}{q_t} = \frac{1}{K_2 e^2} + \frac{1}{q_e} \quad (9)$$

where K_2 (g mg^{-1} min^{-1}) is the rate constant and q_e is the amount of EBT adsorbed over the surface of the nanoparticles at equilibrium (Fig. S11b†). The experimental data indicate that the adsorption rate follows pseudo first-order kinetics for the removal of the dye, due to the higher fitting value of R^2.

4.7. Applicability in real samples and salt effect

To check the applicability of the nanoparticles as an adsorbent in real samples, a variety of water samples was collected and the adsorptive behavior was tested by using them as solvents, instead of distilled water. Water samples from tap, well, tube-well, handpump and canal were used for this purpose. In each water sample, 50 ppm of dye was adsorbed using 50 ppm of nanoparticles and the percentage removal of dye was calculated (Fig. 12a). The results illustrated that EBT was successfully removed for all samples, but with slight reduction in removal efficiency. This could be attributed to interference caused by dissolved salts and low oxygen content in these water samples. This interference of salts was further tested from adsorption batches of dye containing 20 ppm of common salts present in water bodies, such as sodium chloride, nickel acetate, calcium carbonate, zinc sulphate and magnesium chloride (Fig. 12b). The results have shown that dissolved ions impart a small declining effect on the adsorption capacity of the nanoparticles. This decrease was associated with the competitive adsorption behavior of salts over the surface of nanoparticles. As a result, the dye molecules found less adsorption sites over the surface of the nanoparticles.

5. Conclusions

CeO_2 nanoparticles (both bare and surfactant stabilized) can penetrate cells and may interfere with cellular components, causing damage to cell division resulting in the inhibition of the growth of the organism. To summarize, we have shown the genotoxic and growth inhibitory effects of bare and surfactant stabilized CeO_2 nanoparticles, which can be surpassed by using a biocompatible coating over the nanoparticles. The biocompatible coating leads to the enhancement of the size of the nanoparticles and alters the properties, such as making the

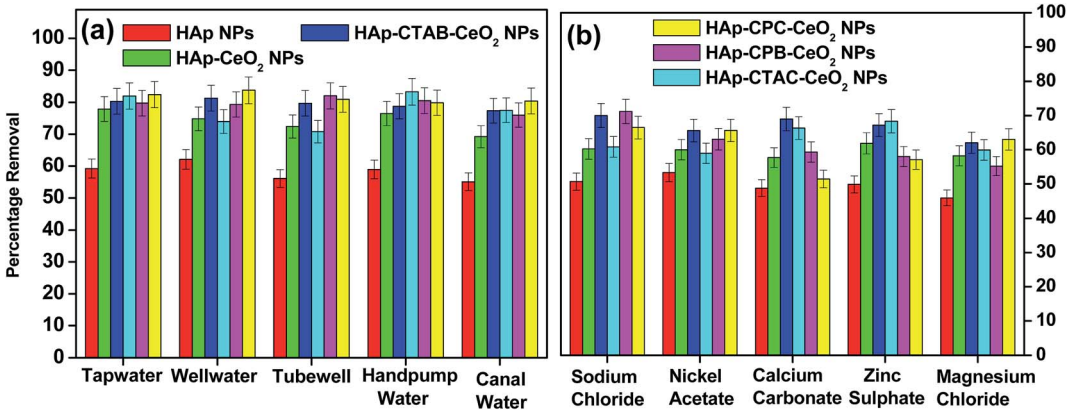

Fig. 12 Effect on percentage dye removal by nanoparticles (a) in different real water samples and (b) in the presence of different salts.

nanoparticles non-toxic. The antiproliferative activity of around 0.00 to 7.7% PIG for HAp coated nanoparticles further enhanced the biocompatibility of as formed nanoparticles. The lower rate of chromosomal aberrations in the case of the HAp coating has clearly signified the biological importance of the as formed nanoparticles. The effect of coating on the surface properties of the nanoparticles was tested by adsorption experiments against EBT dye. The system was optimized with the help of different parameters, including the influence of pH, adsorbent dosage, initial dye concentration and time of contact. The findings show a slight decrease in dye adsorption efficiency by HAp coated nanoparticles, but a huge enhancement in the biocompatibility of the modified system. The prepared HAp/CeO_2 nanohybrids can be exploited to act as competent low-cost adsorbents for removal and recovery of dye from the aqueous environment. This work validates and promotes the idea of using biocompatible and non-toxic nanomaterials for environmental remediation with high efficiency.

Acknowledgements

Savita Chaudhary is grateful to DST Inspire Faculty award [IFA-CH-17] and DST Purse grant II for financial assistance. Priyanka Sharma is grateful to DST India for providing a senior research Inspire fellowship [IF-140267].

References

1 W. H. De Jong and P. J. A. Borm, *Int. J. Nanomed.*, 2008, **3**, 133–149.
2 S. Naahidi, M. Jafari, F. Edalat, K. Raymond, A. Khademhosseini and P. Chen, *J. Controlled Release*, 2013, **166**, 182–194.
3 L. Yu, H. Wang, Y. Zhang, B. Zhang and J. Liu, *Environ. Sci.: Nano*, 2016, **3**, 28–44.
4 C. Walkey, S. Das, S. Seal, J. Erlichman, K. Heckman, L. Ghibelli, E. Traversa, J. F. McGinnis and W. T. Self, *Environ. Sci.: Nano*, 2015, **2**, 33–53.
5 M. Hajjari, M. Ardjmand and M. Tabatabaei, *RSC Adv.*, 2014, **4**, 14352–14356.
6 C. M. Rico, S. C. Lee, R. Rubenecia, A. Mukherjee, J. Hong, J. R. Peralta-Videa and J. L. Gardea-Torresdey, *J. Agric. Food Chem.*, 2014, **62**, 9669–9675.
7 F. Pagliari, C. Mandoli, G. Forte, E. Magnani, S. Pagliari, G. Nardone, S. Licoccia, M. Minieri, P. D. Nardo and E. Traversa, *ACS Nano*, 2012, **6**, 3767–3775.
8 A. Asati, S. Santra, C. Kaittanis and J. M. Perez, *ACS Nano*, 2010, **4**, 5321–5331.
9 F. Piccino, F. Gottschalk, S. Seeger and B. Nowack, *J. Nanopart. Res.*, 2012, **14**, 1109.
10 K. A. Amin, M. S. Hassan, S. T. Awadel and K. S. Hashem, *Int. J. Nanomed.*, 2011, **6**, 143–149.
11 A. Rocca, S. Moscato, F. Ronca, S. Nitti, V. Mattoli, M. Giorgi and G. Ciofani, *Nanomed. Nanotech. Biol. Med.*, 2015, **11**, 1725–1734.
12 V. Selvaraj, N. Nepal, S. Rogers, N. D. P. K. Manne, R. K. Arvapalli, K. M. Rice, S. Asano, E. Fankenhanel, J. Y. Ma, T. Shokuhfar, M. Maheshwari and E. R. Blough, *Data in Brief*, 2015, **4**, 105–115.
13 D. A. Pelletier, A. K. Suresh, G. A. Holton, C. K. McKeown, W. Wang, B. Gu, N. P. Mortensen, D. P. Allison, D. C. Joy and M. R. Allison, *Appl. Environ. Microbiol.*, 2010, **76**, 7981–7989.
14 P. Rosenkranz, M. F. Cruz, E. Conde, M. R. Fernandez, J. Flores, M. Fernandez and J. Navas, *Toxicol. In Vitro*, 2012, **26**, 888–896.
15 Z. Zhang, X. He, H. Zhang, Y. Ma, P. Zhang, Y. Ding and Y. Zhao, *Metallomics*, 2011, **3**, 816–822.
16 R. Rajan, K. Chandran, S. L. Harper, S.-I. Yun and P. T. Kalaichelvan, *Ind. Crops Prod.*, 2015, **70**, 356–373.
17 K. Cheng, Y. Zhu, W. Weng, J. Lin and H. Wang, *Thin Solid Films*, 2015, **584**, 9–12.
18 F. Tang, C. Wang, X. Wang and L. Li, *Colloids Surf., A*, 2015, **485**, 49–54.
19 E. S. Urquiza, F. A. Cardona, E. H. Herman, P. F. Pacheco-García, R. G. Rodríguez, J. L. Coffer, M. E. Mendoza-Alvarez, J. F. Vélez-Ruiz and M. A. Méndez-Rojas, *J. Colloid Interface Sci.*, 2015, **460**, 339–348.
20 T. Ishihara, T. Maeda, H. Sakamoto, N. Takasaki, M. Shigyo, T. Ishida, H. Kiwada, Y. Mizushima and T. Mizushima, *Biomacromolecules*, 2010, **11**, 2700–2706.
21 M. Muthiah, I. K. Park and C.-S. Cho, *Biotechnol. Adv.*, 2013, **31**, 1224–1236.
22 L. S. Acosta-Torres, L. M. López-Marín, R. E. Núñez-Anita, G. H. Padrón and V. M. Castaño, *J. Nanomater.*, 2011, **8**, 941561.
23 F. Hui and J. Lédion, *Eur. J. Water Qual.*, 2002, **1**, 1–27.
24 V. Sreeja, K. N. Jayaprabha and P. A. Joy, *Appl. Nanosci.*, 2015, **5**, 435–441.
25 A. Bhatnagar, E. Kumar and M. Sillanpää, *Chem. Eng. J.*, 2010, **163**, 317.
26 W. Li, D. Liu, J. Wu, C. Kim and J. D. Fortner, *Environ. Sci. Technol.*, 2014, **48**, 11892–11900.
27 M. Li, X. Xiao, R. Liu, C. Chen and L. Huang, *J. Mater. Sci.: Mater. Med.*, 2008, **19**, 797–803.
28 T. Moudakir, K. Djessas and G. Masse, *J. Cryst. Growth*, 2004, **270**, 517–523.
29 R. Kumar, N. M. Sundaram and V. Rajendran, *Int. J. Eng. Sci. Tech.*, 2010, **2**, 2437–2444.
30 C. Piccirillo, C. W. Dunnill, R. C. Pullar, D. M. Tobaldi, J. A. Labrincha, I. P. Parkin, M. M. Pintado and P. M. L. Castro, *J. Mater. Chem. A*, 2013, **1**, 6452–6461.
31 M. Zhu, H. X. Wang, J. Y. Liu, H. L. He, X. G. Hua, Q. J. He, L. X. Zhang, X. J. Ye and J. L. A. Shi, *Biomaterials*, 2011, **32**, 1986–1995.
32 (*a*) S. Chaudhary, P. Sharma, R. Kumar and S. K. Mehta, *Ceram. Int.*, 2015, **41**, 10995–11003; (*b*) S. Chaudhary, A. Sood and S. K. Mehta, *J. Nanosci. Nanotechnol.*, 2014, **14**, 6824–6834.
33 M. Kumari, A. Mukherjee and N. Chandrasekaran, *Sci. Total Environ.*, 2009, **407**, 5243–5246.
34 N. I. M. Nayak and P. Lakshmi, *J. Pharmacol. Pharmacother.*, 2014, **5**, 56–58.

35 S. Pakrashi, N. Jain, S. Dalai, J. Jayakumar and P. T. Chandrasekaran, *PLoS One*, 2014, **9**, e87789.
36 S. K. Mehta, S. Chaudhary, S. Kumar and S. Singh, *J. Nanopart. Res.*, 2010, **5**, 1697–1709.
37 S. K. Mehta, S. Chaudhary and K. K. Bhasin, *J. Nanopart. Res.*, 2009, **11**, 1759–1766.
38 D. Jamwal, G. Kaur, P. Raizada, P. Singh, D. Pathak and P. Thakur, *J. Phys. Chem. C*, 2015, **119**, 5062–5073.
39 C. Walkey, S. Das, S. Seal, J. Erlichman, K. Heckman, L. Ghibelli, E. Traversa, J. F. McGinnisf and W. T. Self, *Environ. Sci.: Nano*, 2015, **2**, 33–53.
40 A. P. Bijelić, M. Mojović, S. Stamenković, M. Jovanović, V. Selaković, P. Andjus and G. Bačić, *Free Radicals Biol. Med.*, 2016, **96**, 313–322.
41 T. Pirmohamed, J. M. Dowding, S. Singh, B. Wasserman, E. Heckert, A. S. Karakoti, J. E. King, S. Seal and W. T. Self, *Chem. Commun.*, 2010, **46**, 2736–2738.